

***Final Draft***  
**of the original manuscript:**

Zeng, R.-C.; Chen, J.; Dietzel, W.; Zettler, R.; dos Santos, J.F.; Nascimento, L.;  
Kainer, K.U.:

**Corrosion of Friction Stir Welded Magnesium Alloy AM50**

In: Corrosion Science (2009) Elsevier

DOI: [10.1016/j.corsci.2009.04.031](https://doi.org/10.1016/j.corsci.2009.04.031)

# Corrosion of Friction Stir Welded Magnesium Alloy AM50

Rong-Chang ZENG <sup>a,\*</sup>, Jun Chen <sup>a</sup>, Wolfgang Dietzel <sup>b</sup>, Rudolf Zettler <sup>b</sup>, Jorge F. dos Santos <sup>b</sup>, M.

Lucia Nascimento <sup>c</sup>, Karl Ulrich Kainer <sup>b</sup>

<sup>a</sup> School of Material Science and Engineering, Chongqing University of Technology, Xingshenglu Rd. 4, Chongqing 400050, China

<sup>b</sup> GKSS-Forschungszentrum Geesthacht GmbH, Max Planck Strasse 1, 21502 Geesthacht, Germany

<sup>c</sup> Technische Universität Berlin, Fachgebiet Werkstofftechnik, Strasse des 17. Juni 135, 10623 Berlin, Germany

---

## ABSTRACT

The microstructure of a friction stir welded magnesium alloy AM50 was examined by means of optical light microscopy. The chemical composition, particularly the iron content, and morphology of the oxide film were analyzed and discerned via auger electron spectroscopy (AES) and X-ray photoelectron spectroscopy (XPS). Corrosion behaviour of the welds and base materials were investigated by virtue of neutral salt spray tests and potentiodynamic polarization measurements in conventional cells and in a mini cell. The results demonstrate that minor increases in iron concentration as might be speculated to occur as a consequence of tool/work piece interaction during the welding process on the corrosion resistance of the weld can be ignored. The corrosion morphology was predominantly influenced by the distribution of the Mg<sub>17</sub>Al<sub>12</sub> phase. Here, it was also found that the corrosion resistance of the friction stir weld varied in response to changes in the joint microstructure.

*Keywords:* A. Magnesium alloy; A. Iron; B. XPS; B. Polarization; C. Corrosion

---

## 1. Introduction

---

\* Corresponding author: Tel/Fax: +86-23-68665616.  
E-mail address: [rczeng2001@yahoo.com.cn](mailto:rczeng2001@yahoo.com.cn) (R.C. Zeng)

Magnesium alloys are promising candidates to replace steel and aluminium alloys in many structural and mechanical applications due to their attractive properties. They have an outstanding stiffness-to-weight ratio, good castability, high damping capacity as well as ease of recyclability [1]. Die cast AM50 is a preferred magnesium alloy used in the automotive industry due to its high ductility. The joining of magnesium components, made from this alloy, is however still limited. Unfortunately, conventional fusion welding of magnesium alloys often produces porosity in the welded joint. This deteriorates both the mechanical properties as well as corrosion resistance [2-3]. Hence, it will be of extreme benefit if a solid state joining process, i.e., one which avoids the bulk melting of the base material, can be developed and implemented for the joining of magnesium alloys.

Friction stir welding (FSW) is a solid-state joining process invented and patented in 1991 by The Welding Institute (TWI) in Cambridge (UK) [3-4]. The FSW process typically exploits a cylindrical and non-consumable tool consisting of a shoulder and a smaller diameter pin, which protrudes from the tool shoulder. The rotating tool is plunged into the joint line between rigidly clamped and abutting work pieces such that the shoulder makes intimate contact with the work piece surface. This results in the pin being completely embedded within the through-thickness of the work pieces but avoiding full penetration of the work pieces [5-6]. The rotating tool initially develops frictional heat during tool plunge. This heat is then complemented through adiabatic shear of a finite volume of material in the close proximity of the tool pin. The combined heat softens this volume of work piece material and, in combination with tool rotation and application of traversing and axial forces, causes the plasticized material to flow from the front to the back of the tool. This transported material then cools down and consolidates to form the solid state joint [3].

A significant advantage of FSW over conventional fusion welding techniques is that it is capable of producing pore-free joints even if the parent cast alloy contains such pores [7]. Magnesium has a very low standard electrode potential; as such it easily undergoes severe attack in aggressive environments. Consequently, considerable attention has been focused on the corrosion behaviour of magnesium alloys [8].

The reason for the poor corrosion resistance of magnesium and its alloys results primarily from two mechanisms [2]: (1) oxide films forming on the surface are not perfect and protective; (2) galvanic or bimetallic corrosion can be caused by impurities and secondary phases, when associated most notably with iron, nickel and copper. It is well known that iron is a detrimental element for magnesium alloys in their ability to resist corrosion [8]. Thus, there is a tolerance limit for the iron content in magnesium alloys. This tolerance limit depends on the level of manganese present. For the aluminium-magnesium alloy AM50A the critical level of iron content is approximately 0.005 wt % [8-9].

Recently, a variety of studies on the corrosion behaviour of magnesium alloys was undertaken [2, 10-12]. Nevertheless, research on corrosion of friction stir welded magnesium alloys is limited within the literature [2, 13]. Magnesium alloys have moreover been demonstrated to have a lower wear and corrosion resistance than most other friction stir welded light alloys [14]. Kannan et al. [6] found that friction stir welded magnesium alloy AZ31 exhibited a higher SCC susceptibility than the base material. At the same time, it was found that the stir zone or weld nugget exhibited a higher and more uniform pitting corrosion resistance than the base material. Skar et al [13] found that the weld nuggets of friction stir welded AM50A and AZ90D alloys had poor corrosion resistance, and suggested that embedded iron contaminants from wear of the tool could be responsible for these

poor corrosion properties of the welds. The present study seems to indicate that this is not the case.

Generally speaking, data from corrosion tests obtained by applying the conventional polarization method require that large quantities of material are tested, since a freshly prepared surface is essential for each test. Furthermore, the surface preparation is time-consuming. In comparison, a mini-cell system (MCS) is a novel approach which demands only a small measuring area for the corrosion analysis and thus can be applied at different locations of the same surface [15-16]. As such, this method together with the conventional electrochemical technique was applied in the current study to examine the electrochemical corrosion behaviour of the AM50 base material and of friction stir welded joints.

The aim of the present paper was to investigate the influence of microstructural variation on the corrosion behaviour of friction stir welded magnesium alloy AM50, and in particular to clarify the influence which the iron content variation has on the corrosion behaviour and thereby to gain better insight into the corrosion mechanisms of friction stir welded magnesium alloys.

## **2. Experimental**

### *2.1 Microstructural observation*

A cast 2.9 mm thick AM50 alloy (5.6-6.4 wt. % Al, 0.26-0.5 wt. % Mn, 0.2 wt. % Zn, Mg, Bal.) was used for this investigation. FSW was performed by the Materials Joining Technology Group at the GKSS-Forschungszentrum Geesthacht GmbH, Germany, using a Tricept TR805 Robot. Samples coming from the friction stir welded plates were ground with SiC paper up to 1200 grit to obtain a flat region between the base material and the welded metal. All samples were cleaned with acetone prior to testing. The specimens were then etched in a solution containing 1.5 g picric acid, 25 ml

ethanol and 5 ml acetic acid together with 10 ml water, and were examined through optical light microscopy. Here, the base material, the thermo-mechanically affected zone, the heat affected zone and the stir zone - denoted as BM, TMAZ and HAZ and SZ - were examined.

## *2.2 Corrosion tests*

### *2.2.1 Salt fog tests*

Two types of samples were tested, one with polished and the other with as-received surfaces which are generally used for assessing the corrosion susceptibility, employing 5 % NaCl salt spray according to the GB 6458-86 standard in an FQY010A type salt spray test chamber. For polished samples, the test duration was 28 h; for as-received samples, the test duration was 4 h and 28 h, respectively.

### *2.2.2 Conventional polarization tests*

The specimens were polished using 2000 grit paper to achieve a mirror finish prior to electrochemical testing. Conventional potentiodynamic polarization tests were then carried out using an EG & G 273 type potentiostat. A three-electrode system was implemented: a saturated calomel electrode (SCE) and a platinum plate were used as reference electrode together with an auxiliary electrode. The scanning voltage was  $\pm 300$  mV relative to the open circuit potential (OCP) with a scan speed of 0.5 mV/s. The tests were conducted using 3.5% NaCl solution at room-temperature. All potentials in the study are quoted with respect to the SCE.

### *2.2.3 Polarization measurements in mini cells*

The test locations in this study are designated as P1, P2, P3 on the top surface and b1, b2, b3 on

the root surface of the butt welded specimens (as shown in Fig.1). Potentiodynamic electrochemical tests were performed in a MCS: a working electrode contacting with a plastic tip having a diameter of 0.5 mm and filled with 3.5% NaCl solution; inside, a saturated calomel electrode (SCE) and a platinum plate were used as reference electrode and auxiliary electrode, respectively. Initially, the variation in OCP with immersion time was measured in the solution for 5 min, and then the potentiodynamic polarization tests were conducted. The scanning potential ranged  $\pm 300$  mV relative to the OCP. In comparison to the conventional cell, the mini cell employed a higher scanning rate of 10 mV/s to thwart rapid attack of the tiny measurement surface. In order to compare the electrochemical results obtained in a mini cell, some electrochemical experiments were performed on a 273 EG & G type Potentiostat using an exposure area of  $2.84 \text{ cm}^2$  and a scanning rate of 0.2 mV/s. All the potentials referred to in this paper are relative to the SCE.

### *2.3 Surface analysis*

X-ray photoelectron spectroscopy (XPS) analysis was performed using a thermo VG ESCALAB 250 photoelectron spectroscopy system with a monochromatic Al  $K_{\alpha}$  and 1486.6 eV radiation source. This instrument was operated at a power of 150 W and with a pass energy of 50.0 eV. Furthermore, auger electron spectroscopy (AES) to was carried out using the same XPS system at a constant retard ratio of 4.0 to more precisely probe the iron content in the film,. This was done using a pass energy of 4.00 eV. Here, three points in each area on the base material and the weld were investigated.

## 3. Results

### *3.1. Microstructural examination*

Fig. 1 shows a cross-sectional view of the weld nugget, which exhibits a basin shape devoid of pores but having a thick oxide layer. The oxides (Fig. 2a) which are present on the weld surface are in this case the result of the elevated temperature generated during the friction process, since they were not seen to be present on the surface of the base material. The various microstructural regions of the weld are shown in Fig. 2b. In comparison to the weld the microstructure of the base material reveals a typical die-cast structure with  $\alpha$ -Mg grains with eutectic (a mixture of  $\alpha$ - and  $\beta$ -phase) on the grain boundary, and the welded zone was characterized by recrystallized equiaxed  $\alpha$ -Mg grains and the intermetallic compound  $\beta$ -Mg<sub>17</sub>Al<sub>12</sub> (Fig. 2c). It can be observed that the Mg<sub>17</sub>Al<sub>12</sub> or  $\beta$ -phase is distributed randomly and un-ordered at the grain boundaries (GBs) (Fig. 2c) in the parent alloy, whereas the  $\beta$ -phase precipitates in the region of the joint experiencing a deformation flow can be seen to be deposited in an orderly manner in the weld nugget (Figs. 2d and 2e, respectively).

### 3.2. Morphology and chemical composition of the oxide film

The as-received surface morphologies of the base material and the weld zone are shown in Figs. 3a and 3b, respectively. It is obvious that some island-chain-like oxides, caused by the original extrusion process, formed on the smooth surfaces of the work pieces. In comparison, this oxide array is interrupted by the plastic deformation induced via contact between the rotating and traversing tool shoulder with the surface of the work piece material. Furthermore, surface roughness or irregularities are seen to increase, and grooves or bands are evident to have formed (Fig. 3b).

An investigation of the chemical composition of the oxide film was made by means of XPS and AES. Figs. 4a and 4b depict the XPS spectra of the base alloy and the weld zone, respectively. The chemical composition of the oxide films on both the base material and the FSW zone obtained with XPS after 30 s etching is given in Table 1. It becomes evident through this method of investigation

that the surface layer consists of (Mg, Al) oxides and that a trace of iron exists in both the base alloy and the weld.

The spot sizes employed for AES and XPS were approximately 100 nm and 500 μm, respectively. Thus, AES could be employed to detect the composition of smaller spots. Figs. 5a and 5b depict the AES spectra of the base material and the FSW zone, respectively. Table 2 contains the chemical composition of FSW zone determined by AES at point 2 in Fig. 3b. A trace of Fe was detected only at point 2, located in the region where material bending caused by the shoulder during the welding process had occurred. Fe was not detected at any of the other five points. Consequently, it is proposed that this trace of increase in iron content is the result of an interaction between the rotating tool and the flowing material.

### 3.3. Corrosion morphology

Fig. 6 shows the micrograph of a polished specimen after 28 hours salt spray corrosion testing. Here, it can be seen that the majority of the welded joint was not attacked except for localized narrow areas, very likely associated with the distribution of the  $\beta$ -phase (Fig. 6a). In contrast, serious general corrosion could be observed to have occurred on the BM (Fig. 6b). Further investigation revealed that inter-granular corrosion fissures were initiated in the base material along the GBs (Fig. 6c), where the  $\beta$ -phase is distributed, while trans-granular fissures could also be seen in the grain interiors (Fig. 6c).

In the case of the as-received sample after 4 hours salt spray test a distinctly different corrosion morphology was observed (Fig. 7). Here, the sample suffered pitting corrosion and filiform corrosion (Fig. 7a). Filiform corrosion is a thread-like form of corrosion that occurs under organic coatings. The source of initiation is usually a defect or mechanical scratch in the coating. It can be

observed that pitting corrosion and filiform corrosion on the weld dominantly follow the irregularities or scratch direction produced by the FSW process (Figs.7a and 7b). In the case of the BM, cellular corrosion, which consists of filiform corrosion, was macrographically observed (Fig. 7c). A micrographic view (Fig. 7d) demonstrates that the filiform corrosion comprises numerous micro-corrosion pits.

A further investigation of the corrosion morphology exhibits that the base material experienced uniform or general corrosion (Fig. 8a) on the as-received sample after the 28 hours salt spray test, while the weld surface suffered from localized corrosion along surface irregularities (Fig. 8b).

The corrosion products, analyzed with EDS (Fig. 8c), were mainly  $Mg(OH)_2$ . Analogous results were obtained in our prior study [17] and the others [18], where the corrosion morphology either in the base material or in the weld could be attributed to the distribution of  $\beta$ -phase in the microstructure. It may be concluded from Fig. 2 that the corrosion products seem to disperse along the friction stir processing marks left behind by the interaction of the tool with the work piece, and that it is associated with the distribution of  $\beta$ -phase in the weld. Here, the corrosion resistance of the weld having thicker oxide layers appears to be higher than that of the base material.

### *3.4. Corrosion behaviour*

The polarization curves of the BM and for the weld, obtained using the electrochemical cell, are shown in Fig. 9. The corrosion rates of the welded joint and the BM were  $22.2 \mu A/cm^2$  and  $95.1 \mu A/cm^2$ , respectively. The free corrosion potentials ( $E_{corr}$ ) of the welded joint and the BM corresponded to  $-1520$  mV and  $-1553$  mV, respectively. It is apparent that the corrosion resistance of the welded joint is higher than that of the BM and results from the finer grain structure which evolves in this region. It has previously been demonstrated that the corrosion resistance of

magnesium alloys can be improved through grain refinement [8, 19]. Additionally, the increasing volume fraction of  $\beta$ -phase in the welded joint in combination with the finer grains means that the  $\beta$ -phase works as a barrier to general corrosion of magnesium alloys. Consequently, the welded joint had a better corrosion resistance than the BM.

Potentiodynamic polarization measurements with the MCS were employed to further compare the corrosion behaviour of the different zones in the friction stir welded joint. The potential vs. time curves (Fig. 10) of P3, P4, P5 and P6 (Fig. 1) coming from the top polished surface and measured by in the mini cell were relatively close to each another. The potential can be seen to decrease in the order: P1 > P3 > P4 > P5 > P6 > P2. This means that the  $E_{\text{corr}}$  in the HAZ (P2) is the lowest in the joint and the base material. Polarization curves (Fig. 11) again coming from the top surface of the AM50 weldment measured by the mini cell show wide passivity regions. The electrochemical parameters of the measurements performed at various position on the friction stir welded AM50 are compiled in Table 3. It can be seen from this table how  $E_{\text{corr}}$  and the breakdown potential,  $E_b$ , of the weld changed. The  $E_b$  value of the HAZ (P2) is the highest and the corrosion rate is the second lowest after the  $I_{\text{corr}}$  measured at P6 (SZ), which is the lowest. The  $I_{\text{corr}}$  values given in Table 3 illustrate that the corrosion rate of the BM was higher than that of the weld. It should be noted here that this result is in complete agreement with the data for the corrosion rate shown in Fig. 9.

Potentials as a function of immersion time and polarization curves for the weld root surface measured by the mini cell are displayed in Figs. 12 and 13, respectively. The electrochemical parameters of the root surface are indicated in Table 4. The curves shown in Fig. 12 are fairly different from those shown in Fig. 10. Initially, the potentials on the top surface increased rapidly with increasing immersion time. However, after an inflection they slowly approached a steady value.

It can be seen from Fig. 13 that the corrosion rate of the TMAZ (b1) was considerably higher than that of the HAZ (b2, b3, b4 and b5).

Comparing Table 3 and Table 4, it can be seen that the corrosion rate in the HAZ was smaller than that in the TMAZ. This is also supported by the change in morphology as confirmed in Fig. 6, where the HAZ region neighbouring the weld TMAZ is visibly less attacked than the TMAZ. Consequently, it can be stated that the corrosion rates of the friction stir welded AM50 alloy decreased in the order: BM, TMAZ, HAZ and SZ.

## **4. Discussion**

### *4.1. Influence of the microstructure on the corrosion behaviour*

The corrosion morphology of magnesium alloys is considerably influenced by the distribution and amount of  $\beta$ -phase in the microstructure. Although it can be seen from Fig. 6a that most of the surface of the welded joint was not corroded, the linear localized corrosion morphology followed the likely distribution of the  $\beta$ -phase along the GBs. Fig. 6c reveals inter-granular cracks along the  $\beta$ -phase in the GBs of the BM. Similar corrosion morphologies were also found in the magnesium alloy AZ91 [18, 20]. Our previous study [17] also showed that inter-granular attack progressed preferentially and predominantly along the bulk  $\beta$ -particles in the grain boundaries of as-extruded AZ80. Chen et al. [18, 20] claimed hydrogen diffusing to the interior of the matrix, enriching and forming hydrides at the  $\beta$ -phase, and suggested that the cracking of the  $\beta$ -phase resulted from the synergistic effects of hydrogen pressure and expansion stress due to the formation of magnesium hydride in the  $\beta$ -phase.

The corrosion morphologies of the presently investigated AM50 alloy are different from the results obtained for die-cast AM50H and AM20 [19]. Wei et al. [19] found that corrosion pits originated at Mn-containing particles and that the  $\alpha$ -matrix was attacked in the form of fissures which started at pits and propagated in a crooked path to avoid the high Al areas. Interestingly, the  $\beta$ -phase was not affected by the formation of corrosion pits and fissure propagation due to Al segregation in the  $\alpha$ -Mg matrix resulting from non-equilibrium solidification during die-cast process. Accordingly, unlike Al-segregations which appear to dominate the corrosion morphology of die-cast AM50H, the  $\beta$ -phase in the friction stir welded-AM50 alloy appears to play the most important role.

Regarding the influence of the microstructure on the corrosion rate of magnesium alloys, a die-cast alloy with finer grains generally shows a corrosion resistance which is superior to that containing coarser grains [21]. Song et al. [21] studied the corrosion of magnesium alloy AZ91 and suggested that the  $\beta$ -phase mainly served as a galvanic cathode and accelerated the corrosion process of the  $\alpha$ -matrix if the volume fraction of  $\beta$ -phase was small; while for a high volume fraction, the  $\beta$ -phase acted as an anodic barrier to inhibit the overall corrosion of the alloy. It is evident from Fig. 2 that a high volume fraction of  $\beta$ -phase was present in the weld and in the base material. Hence, the  $\beta$ -phase acted as an anodic barrier to prevent overall corrosion. The corrosion resistance in the weld was higher than in the base material owing to the fact that the weld possesses finer grains than the base alloy.

#### *4.2. Influence of iron content on corrosion*

Table 2 shows that the iron content increases from 0.52 at % to 0.90 at % after 30 s etches. The increase in iron content most likely comes from the wear of the tool shoulder brought about by partial melting of the  $\beta$ -phase (at around 430°C), which if present in sufficient quantities causes iron

from the tool to dissolve. This is because the  $\beta$ -phase is aggressive to steel, and iron is easily dissolved [13].

The trace of iron found to occur in the weld has no obvious influence on the corrosion morphology and on the corrosion rate. First of all, minor quantities of iron were detected only at point 2 in Fig. 3, located in the bend caused by the shoulder action during the welding process, and no such traces were detected for any of the other (five) measuring points. This is regardless of the calculation error for the iron content due to a higher background noise. Moreover, the corrosion morphology in Fig. 6a is not the same as observed by Skar [13] in the weld zone of AZ91D and AM50A where it was found that the corrosion attack was localized in the weld from one end of the weld to the midpoint of its length. In some regions, there was perforation of the samples, whereas no analogous corrosion morphologies were perceived in the present study. Furthermore, the corrosion rate of the weld could be seen to be lower instead of being higher than that of the base material. Consequently, the influence of a minor increase in iron concentration on the corrosion morphology and corrosion resistance of the current welds will not be significant.

## 5. Conclusions

(1) The welds were not contaminated with traces of iron as purported in the literature to occur as a result of wear from the FSW tool. The influence of a slight increase in iron concentration had no effect on the corrosion resistance of the weld and thus can be ignored.

(2) The corrosion morphology of the AM50 alloy was predominantly controlled by the  $\beta$ -phase distribution. Intergranular corrosion was discerned in the base material, whereas pitting corrosion and filiform corrosion occurred in the welds.

(3) The corrosion rates varied across the different friction stir weld zones. They were found to be higher in the base material than in the weld. Similarly, the thermo-mechanically affected zone was found to be more susceptible to corrosion attack than the heat affected zone of the joint. The corrosion resistance of the various zones increased in the order: BM, TMAZ, HAZ and SZ.

### **Acknowledgements**

The authors gratefully acknowledge the technical support extended by Mr. U. Burmester, Mr. V. Kree, and Ms. P. Fischer in GKSS Forschungszentrum Geesthacht GmbH during the course of this work, and the work is partially supported by the foundation of CSTC, 2008BB0063.

### **References**

- [1] R. C. Zeng, W. Dietzel, R. Zettler, J. Chen, K. U. Kainer, *Nonferrous Met. Soc. China* 18 (2008) s76-s80.
- [2] R. C. Zeng, J. Zhang, W. J. Huang, W. Dietzel, K. U. Kainer, C. Blawert, W. Ke, *Trans. Nonferrous Met. Soc. China*.16 (2006) s763-s771.
- [3] T. Nagasawa, M. Otsuka, T. Yokota, T. Ueki, Structure and mechanical properties of friction stir weld joints of magnesium alloy AZ31, in: H. I. Kaplan, J. Hryn, B. Clow (Eds.), *Magnesium Technology 2000*, TMS, Warrendale, 2000, pp.383-387.
- [4] S. W. Kalle, W. M. Thomas, E. D. Nicholas, in: K. U. Kainer (Ed.), *Weiheim, Wiley-VCH Verlag GmbH*, 2000, pp.175-190.
- [5] R. Zettler, A. C. Blanco, J. F. dos Santos, S. Marya, The effect of process parameters and tool geometry on thermal field development and weld formation in friction stir welding of the alloy AZ31 and AZ61, in: N. R. Neelameggham, H. I. Daplan, B. R. Powell (Eds.), *Magnesium*

- Technology, TMS, San Francisco, 2005, pp. 409–423.
- [6] M. B. Kannan, W. Dietzel, R. Zeng, R. Zettler, J. F. dos Santos, *Mater. Sci. & Eng. A* 460–461(2007) 243.
- [7] L. Commin, J. E. Masse, M. Dumont, L. Barrallier, Microstructure features of hot rolled AZ31 magnesium alloy for friction stir welding, in: K. U. Kainer, (Ed.), *Proceedings of the 7th international conference on magnesium alloys and their applications*, Weiheim, Wiley-VCH Verlag GmbH, 2006, pp.877-882.
- [8] G. Song, A. Atrens, *Adv. Eng. Mater.* 1 (1999) 11.
- [9] M. M. Avedesian, H. Baker, *Magnesium and Magnesium Alloys*, ASM International, Materials Park, OH, 1999.
- [10] G. Song, A. Atrens, *Adv. Eng. Mater.* 5 (2003)837-858.
- [11] G. Song, *Adv. Eng. Mater.* 7(2005)563-586.
- [12] J. Chen, J. Q. Wang, E. H. Han, W. Ke, *Corrosion Sci.*50 (2008)1449-1459.
- [13] J. I. Skar, H. Gjestland, L. D. Oosterkamp, D. L. Albright, *Magnesium Technology*, TMS, North Carolina, 2004, pp.25-30.
- [14] G. Govender, J. H.Ferreira, In: E. Aghion, D. Eliezer (Eds.), *Magnesium 2000*, Magnesium Research Institute LTD, Beer-Sheva, 2000, pp.371-376.
- [15] M. Nascimento, W. Müller, A. Carvalho, H. Tomás, *Dental Materials* 23 (2007)369-373.
- [16] W. D. Müller, K. Ibendorf, *Analytical and Bioanalytical Chemistry* 349(1994)182-184.
- [17] R. C. Zeng, E. H.Han, W. Ke, *J. Mater. Sci & Techno.* 23(2007)353-358.
- [18] J. Chen, J. Q. Wang, E. H. Han, J. H. Dong, W. Ke, *Corrosion Sci.* 50 (2008)1292-1305.
- [19] L. Y. Wei, H. Westengen, T. K. Aune, D. Albright, in:H .I. Kaplan, J. N. Hryn, B. B. Clow

(Eds.), Magnesium Technology 2000, TMS, Warrendale, PA, 2000, pp.153-160.

[20] J. Chen, J. Q. Wang, E. H. Han, W.Ke, Mater. Sci & Eng A 488(2008)428-434.

[21] G. Song, A. Atrens, X. Xu, Z. Bo, B. Zhang, Corr. Sci. 40(1998)1769-1791.

## Captions

### Figures

Fig.1 Cross-section view of an FSW-AM50 sample. Note: numbers 1, 2, 3...are locations measured in mini cells. (a-unaaffected material, b-heat affected zone (HAZ), c-thermo-mechanically affected zone (TMAZ) and d-stir zone).

Fig.2 Microstructure of (a) cross-sectional view of the nugget, (b) the weld, (c) the base or parent material (BM or PM), (d) weld zone at the vicinity of PM, and (e) the stir zone. Magnesium<sub>17</sub>Al<sub>12</sub> or  $\beta$ -phases shown as the arrows are distributed with the solid flow shape.

Fig. 3 As-received surface morphology of (a) the base material and (b) FSW zone. The number 1, 2 and 3 are the probe sites for AES.

Fig.4 XPS spectrum for (a) the base alloy and (b) FSW zone.

Fig.5 Survey spectrum of AES (a) the base material and (b) FSW zone, a trace of Fe was detected at point 2 in Fig.3b.

Fig. 6 Corrosion morphologies: (a) Less attack in the weld zone, (b) serious uniform attack in base material, (c) intergranular corrosion in base material after 28 h salt spray corrosion test.

Fig.7 Corrosion morphology of (a) the weld and the base material, (b) the weld, (c) the base material, and (d) the magnification of Fig.7c on the as-received sample after the 4 h salt spray performance.

Fig.8 (a) Macro-corrosion morphology, (b) SEM of the weld, and (c) EDS of the corrosion products in the weld after the 28 h salt spray performance, indicating that it mainly consisted of  $Mg(OH)_2$ .

Fig.9 Polarization curves of the base alloy and the weld.

Fig.10. Potential versus time of the full face of FSW-AM50 in mini cells.

Fig.11. Polarization curves of FSW-AM50 on the welding surface in mini cells.

Fig.12. Potential as a function of time for the weld root surface in mini cells.

Fig. 13. Polarization curves of the weld root surface in mini cells.

## Tables

Table 1 Chemical compositions by XPS, at. %; etch time (30s).

Table 2 Chemical compositions at point 2 in Fig.3b of FSW zone by AES, at. %.

Table 3 Electrochemical response of various positions on top surface.

Table 4 Electrochemical parameters of root surface.

Tables

Table 1

Material	C 1s	O 1s	Fe 2p	Mg 1s	Al 2p
FSW zone	29.77	36.75	0.90	26.49	6.10
Base material	11.56	48.66	0.52	31.64	7.62

Table 2

Etch Time (s)	C KL1	O KL1	Fe LM2	Mg KL2	Al KL1
100	52.5039	17.3759	2.99201	22.4116	4.71668
200	19.7917	35.7226	5.49784	31.5928	7.39515

Table 3

Positions	P1	P2	P3	P4	P5	P6
Regions	BM	HAZ	TMAZ	TMAZ	TMAZ +SZ	SZ
$I_{corr} / \mu A/cm^2$	36.9	6.2	9.7	8.3	7.8	5.6
$E_{corr}/mV$ vs. SCE	-1534	-1588	-1574	-1541	-1552	-1563
$E_b/mV$ vs. SCE	-1366	-1169	-1289	-1450	-1220	-1362

Table 4

Positions	b1	b2	b3	b4	b5
Regions	TMAZ	HAZ	HAZ	HAZ	HAZ
$I_{corr} \mu A/cm^2$	70.7	14.5	10.1	4.9	8.3
$E_{corr}/mV$ vs. SCE	-1450	-1417	-1348	-1439	-1464

Fig.1

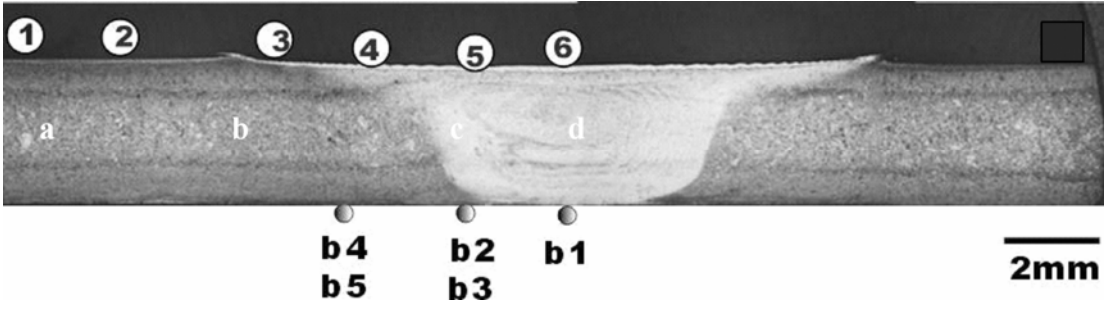


Fig.2a

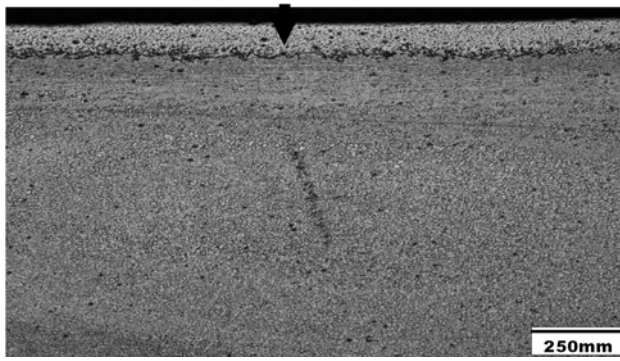


Fig.2b

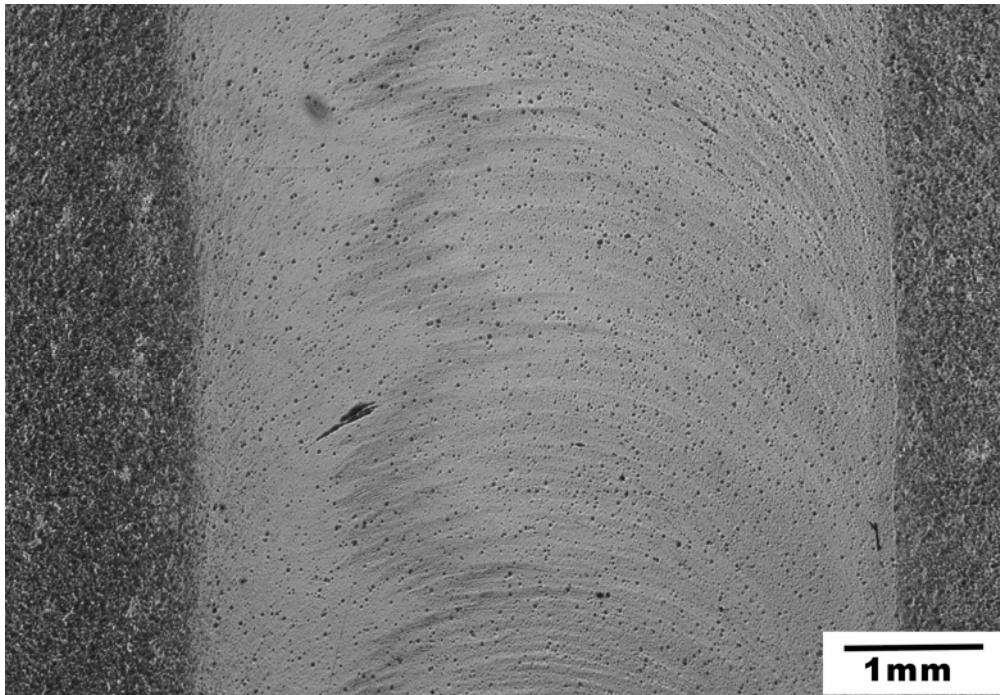


Fig.2c

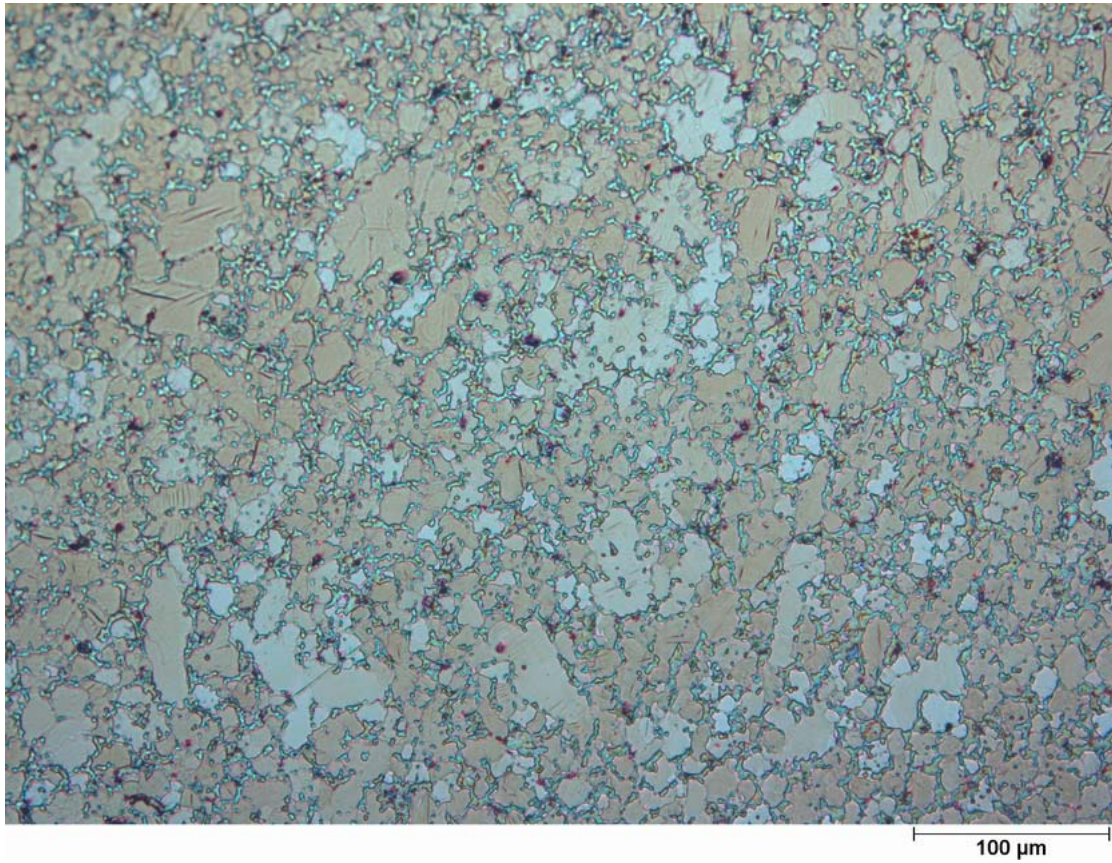


Fig.2d

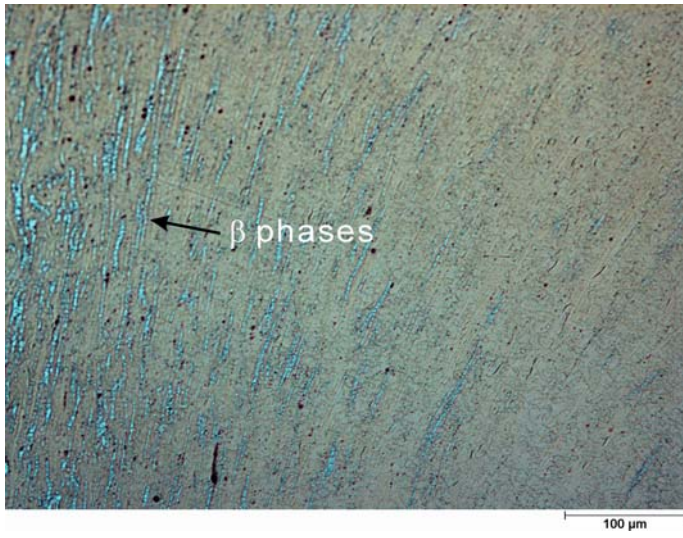


Fig.2e

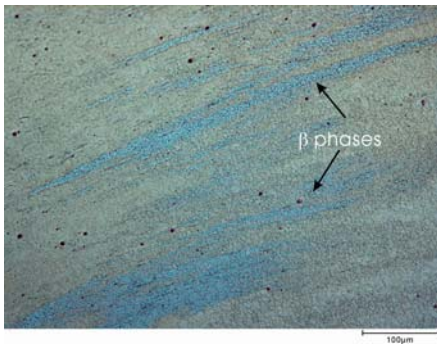


Fig.3a

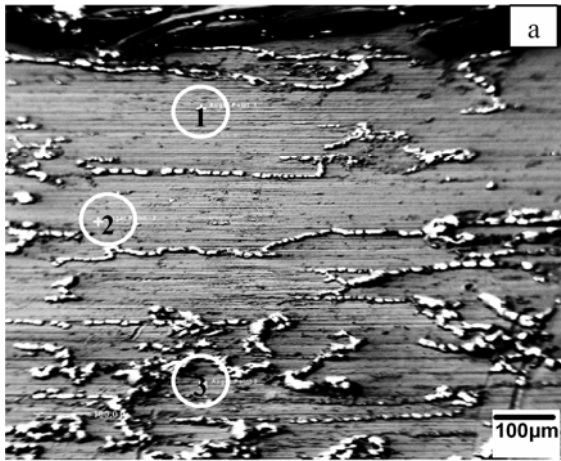


Fig.3b

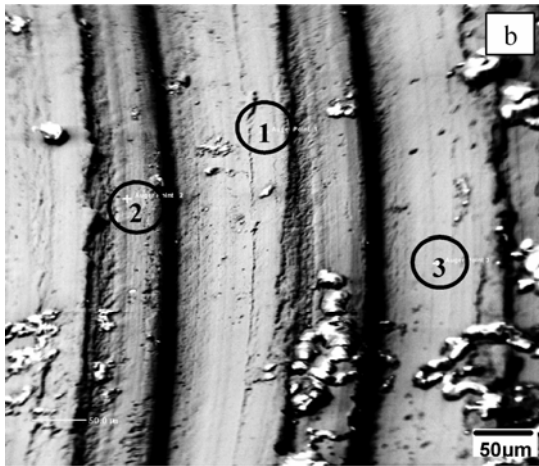


Fig.4a

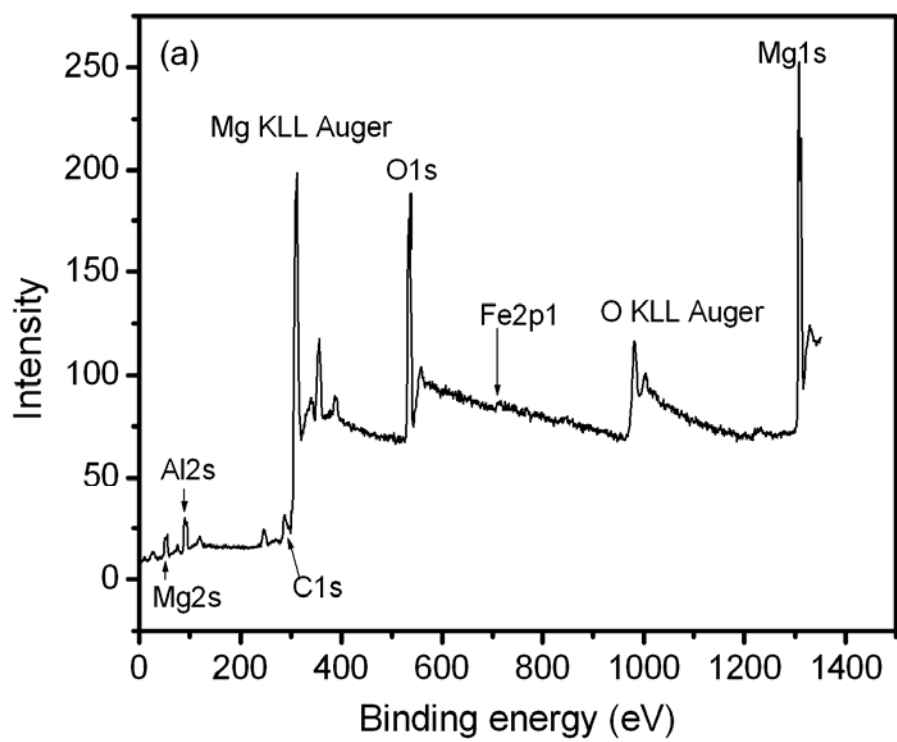


Fig.4b

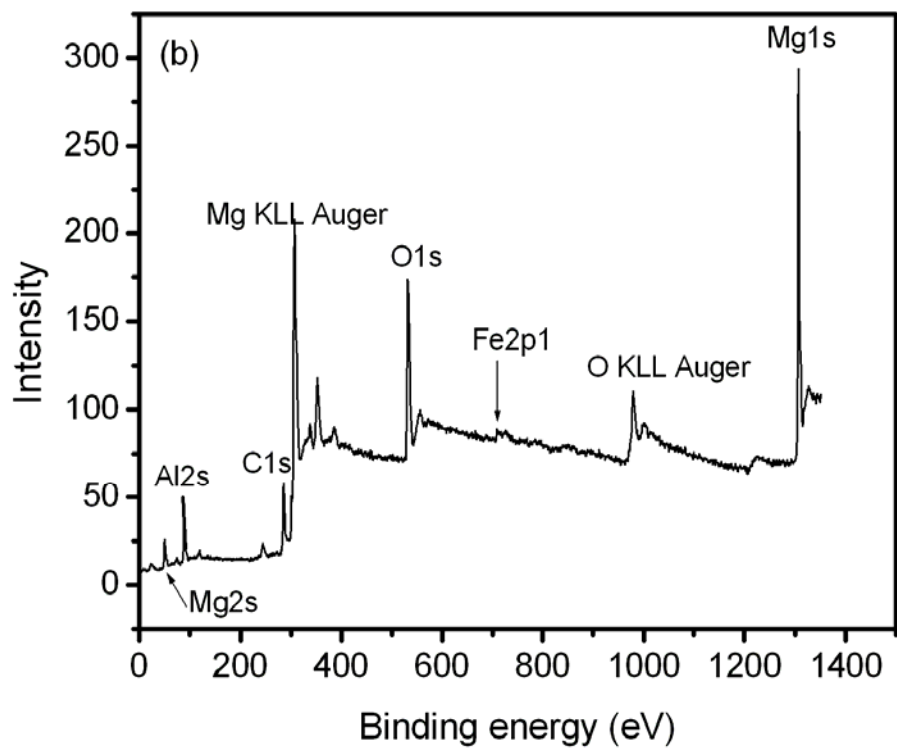


Fig.5a

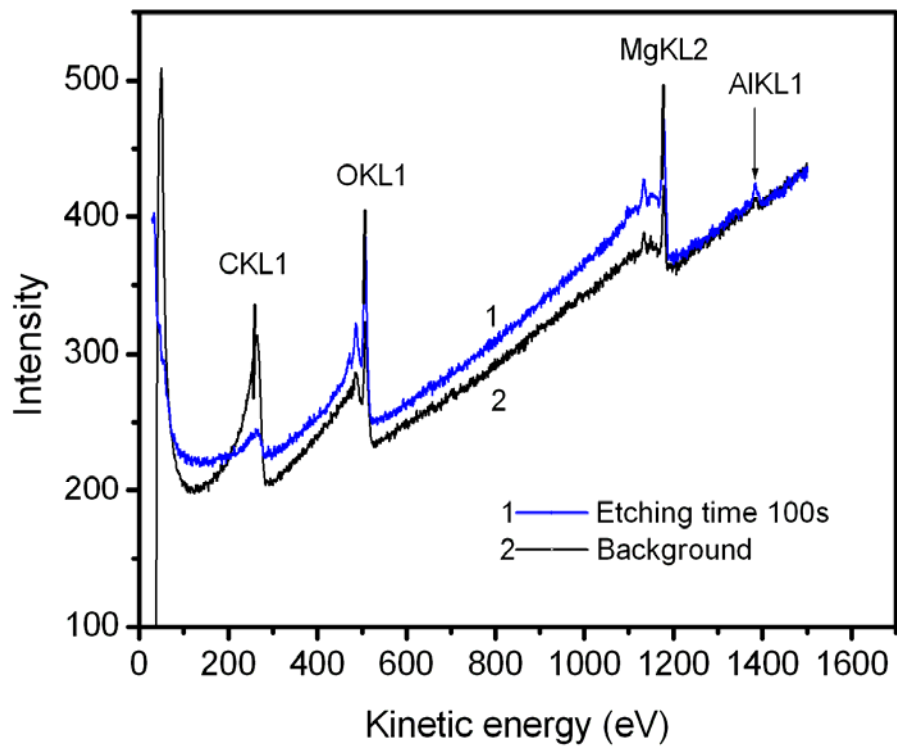


Fig.5b

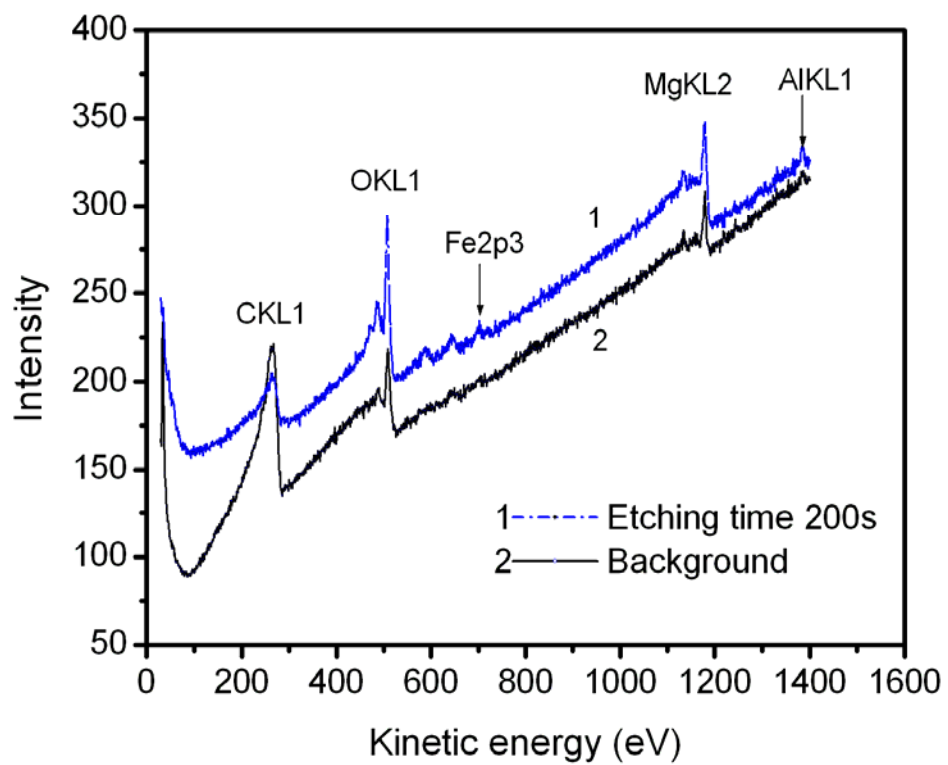


Fig.6a

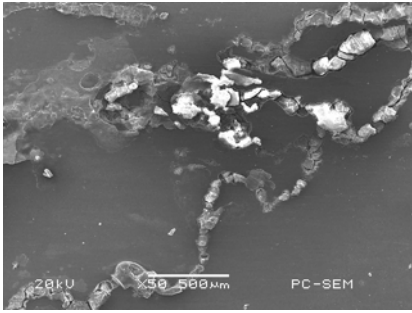


Fig.6b

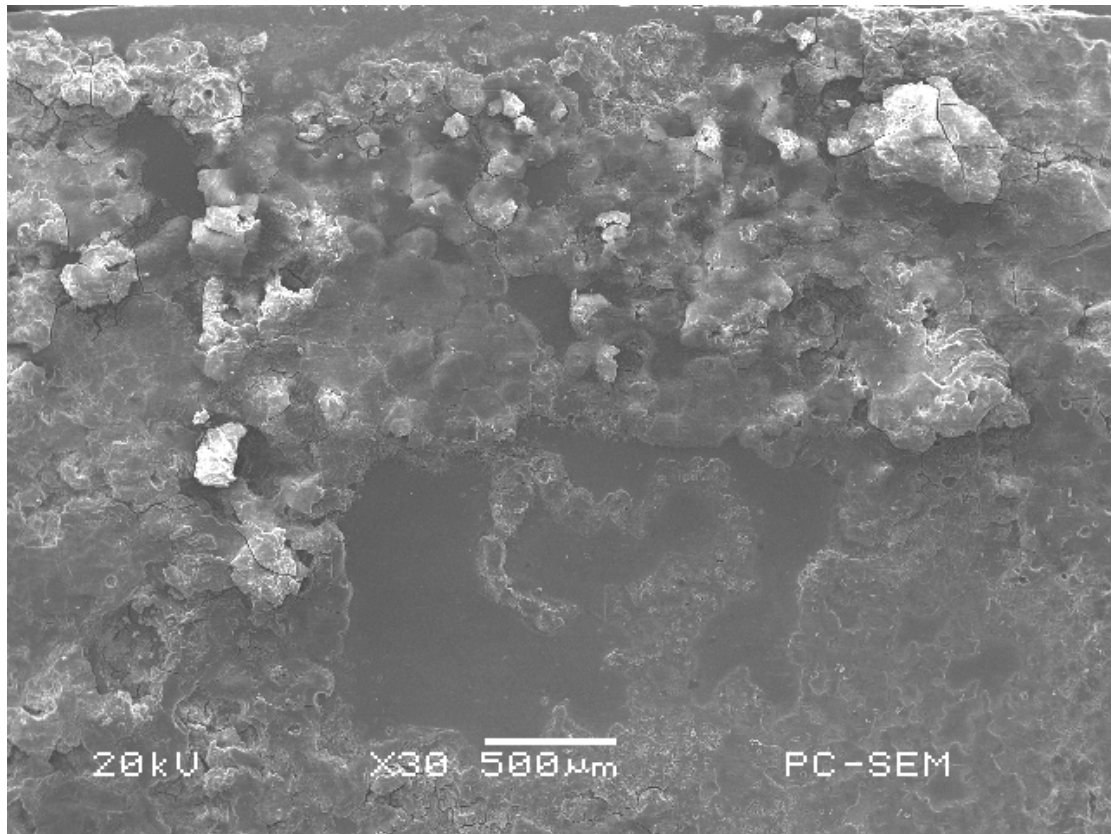


Fig.6c

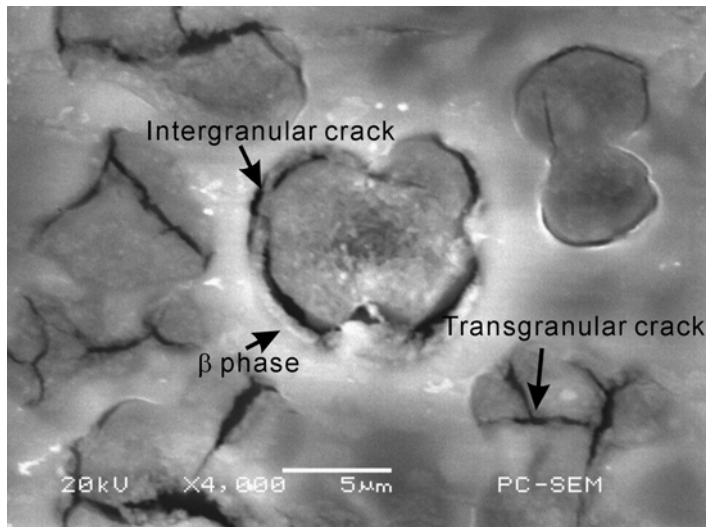


Fig.7a

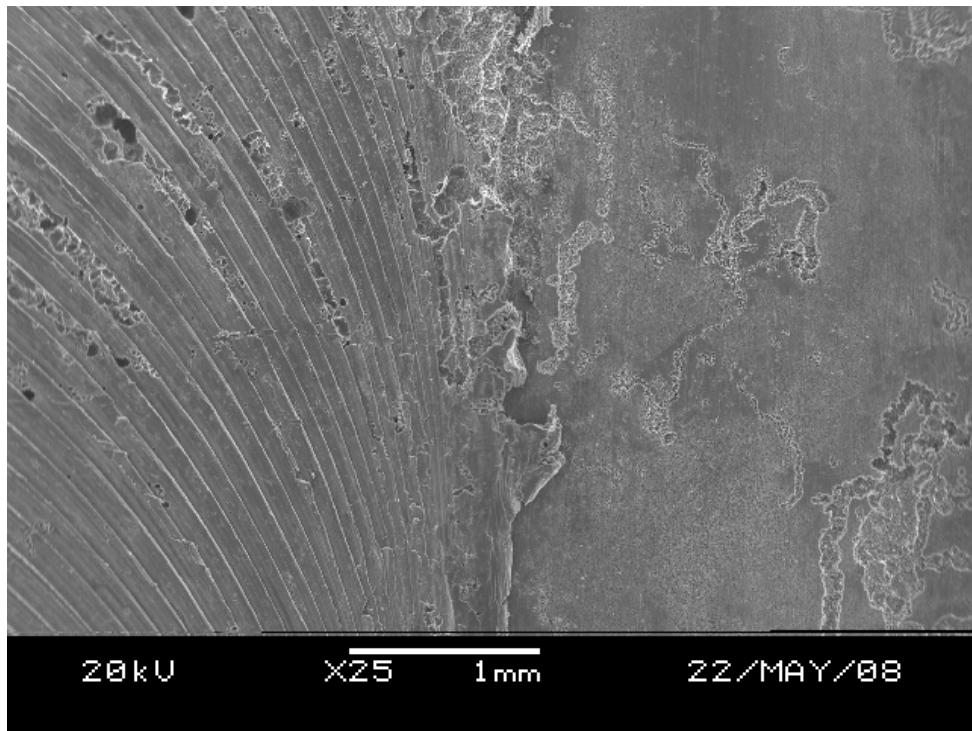


Fig.7b

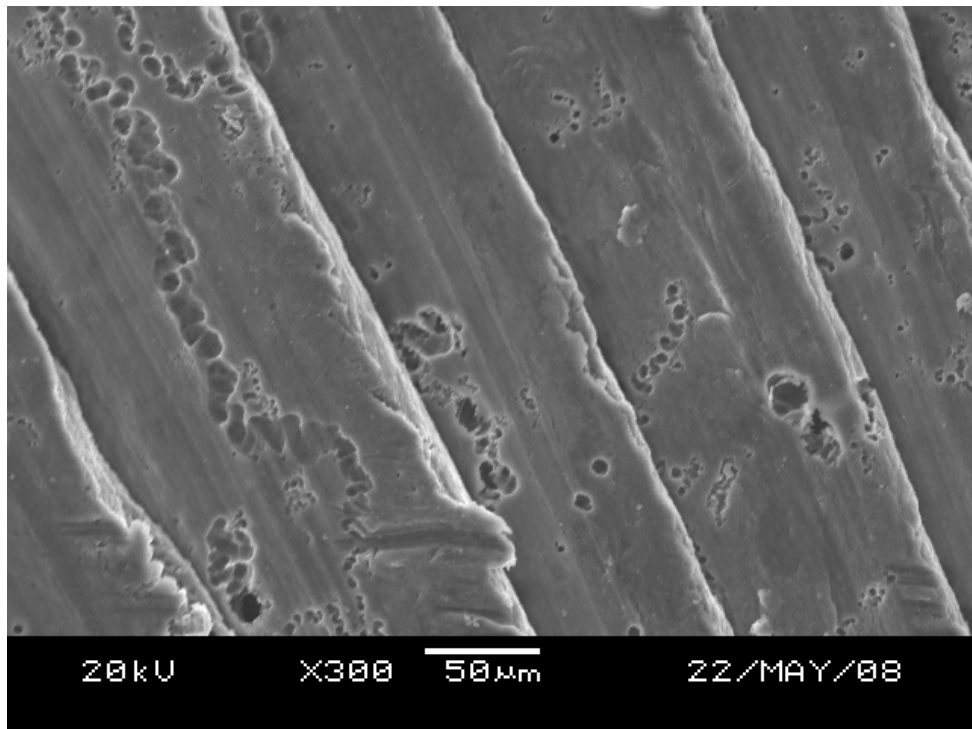


Fig.7c

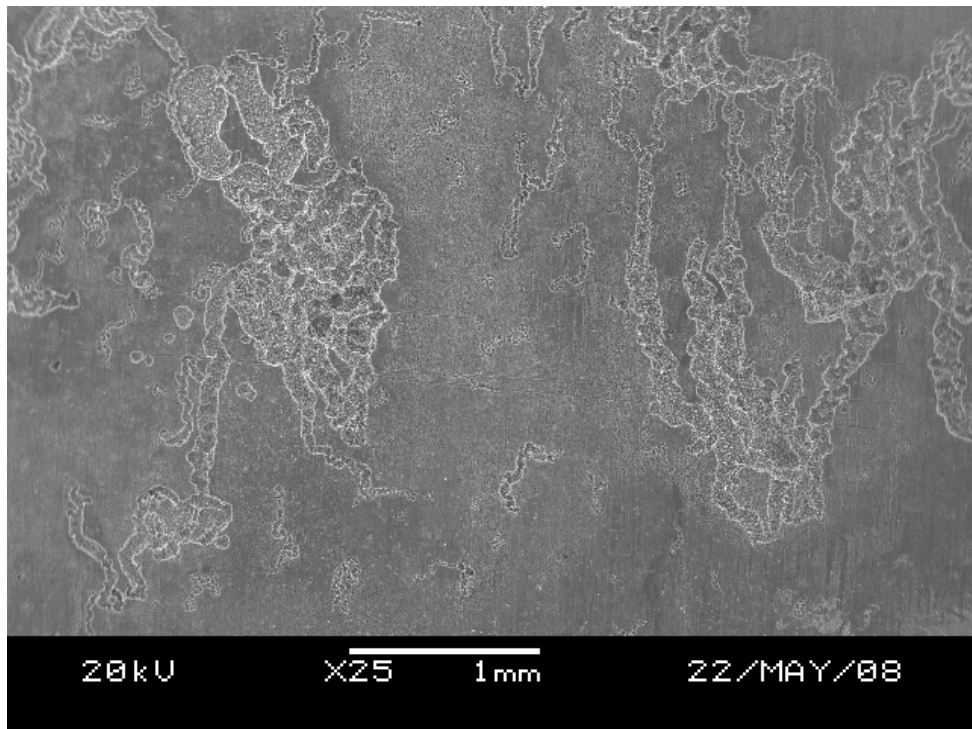


Fig.7d

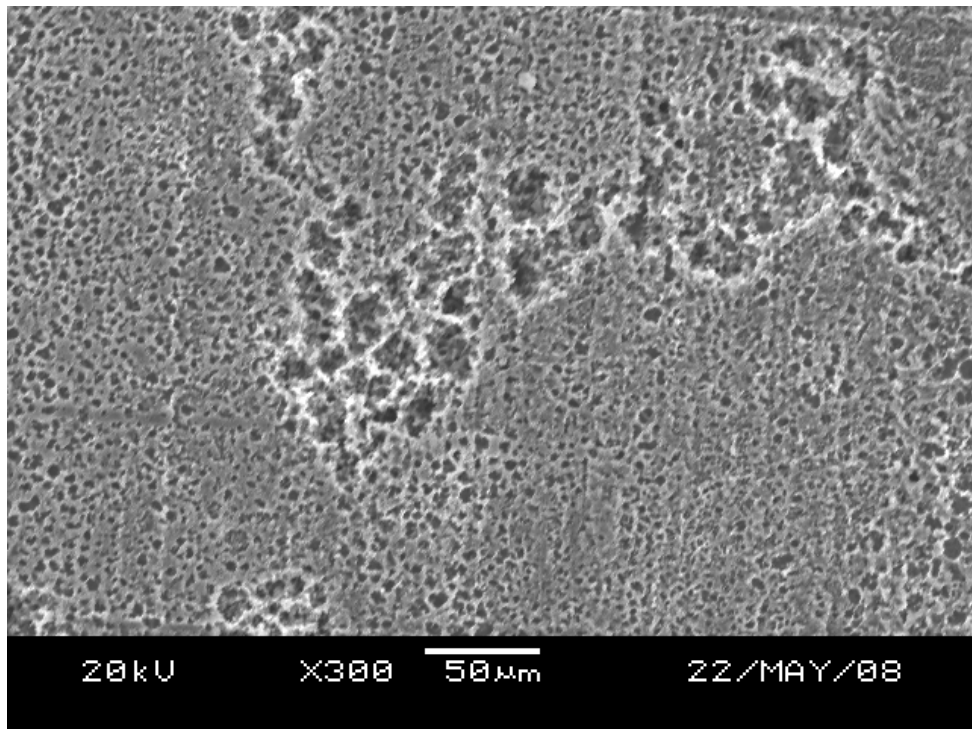


Fig.8a

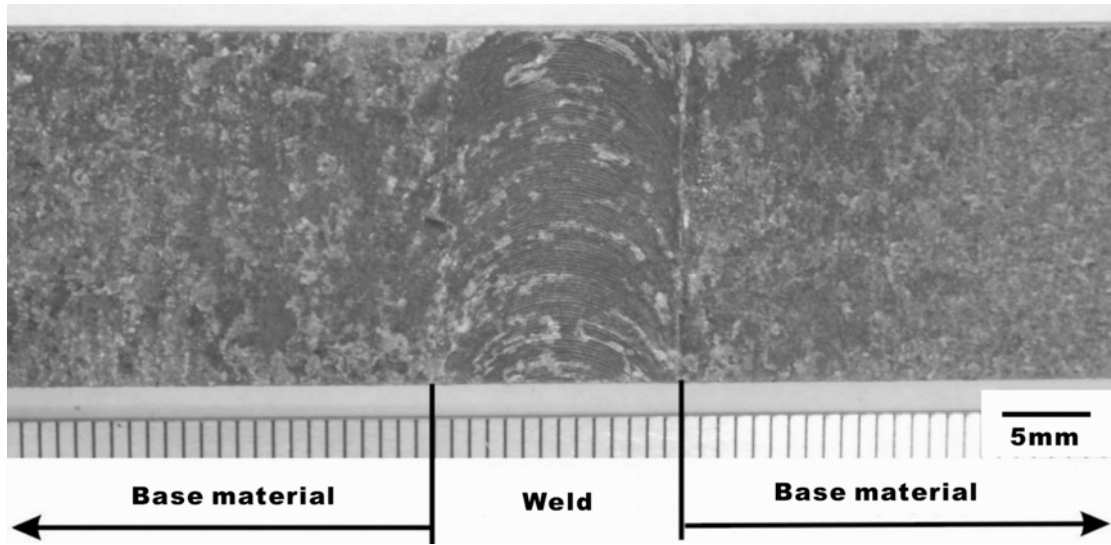


Fig.8b

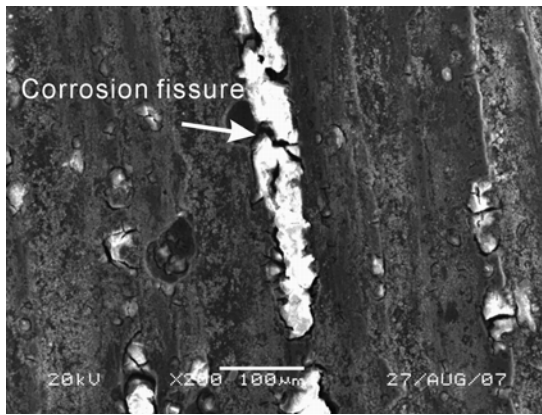


Fig.8c

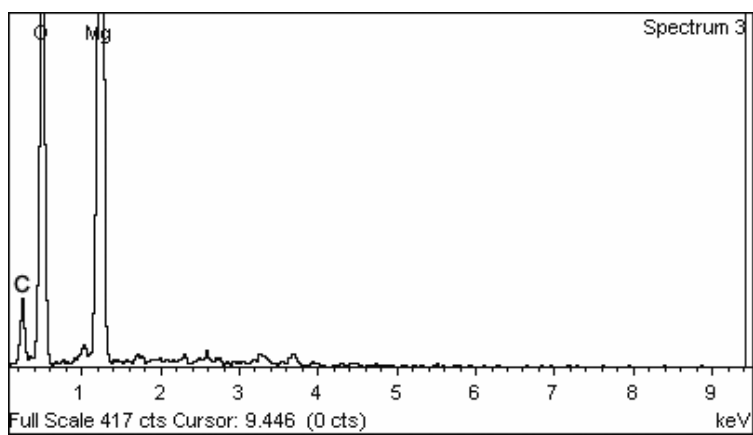


Fig.9

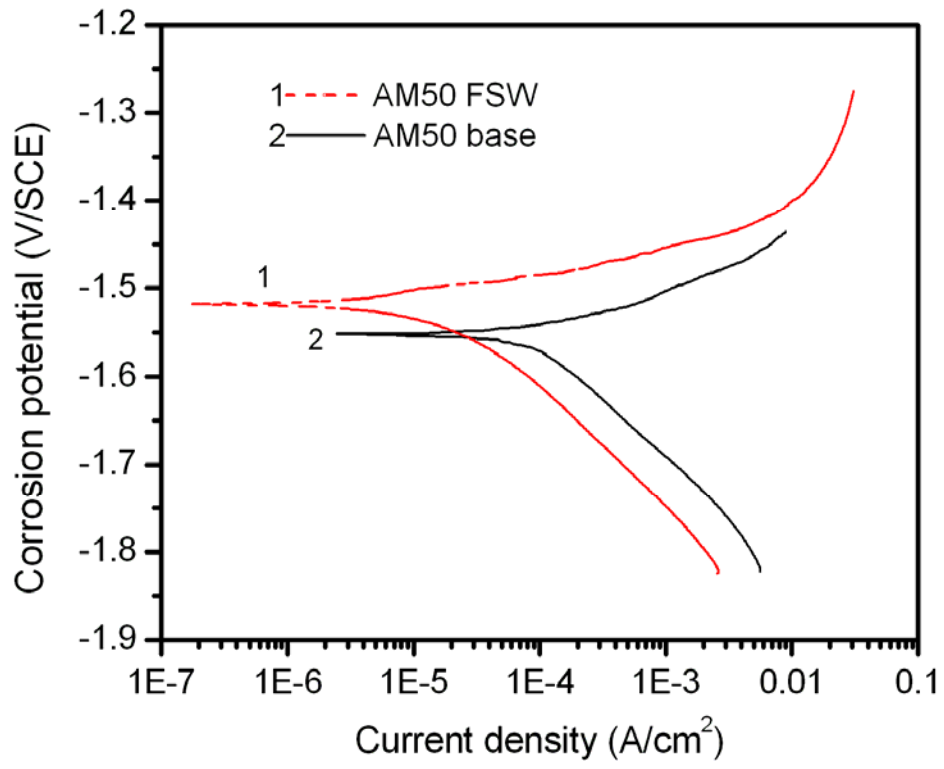


Fig.10

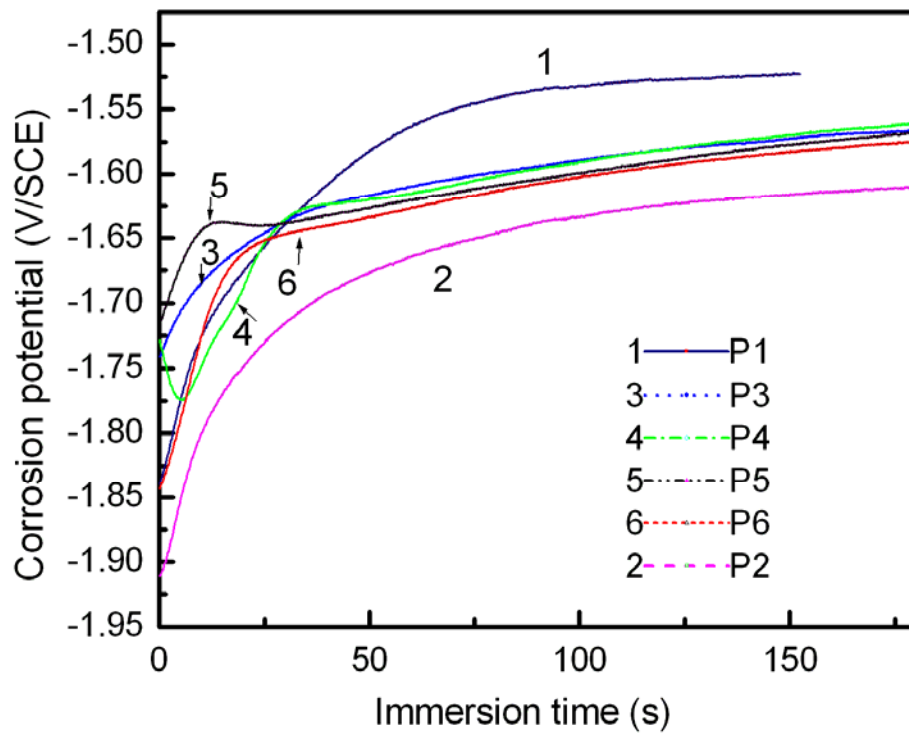


Fig.11

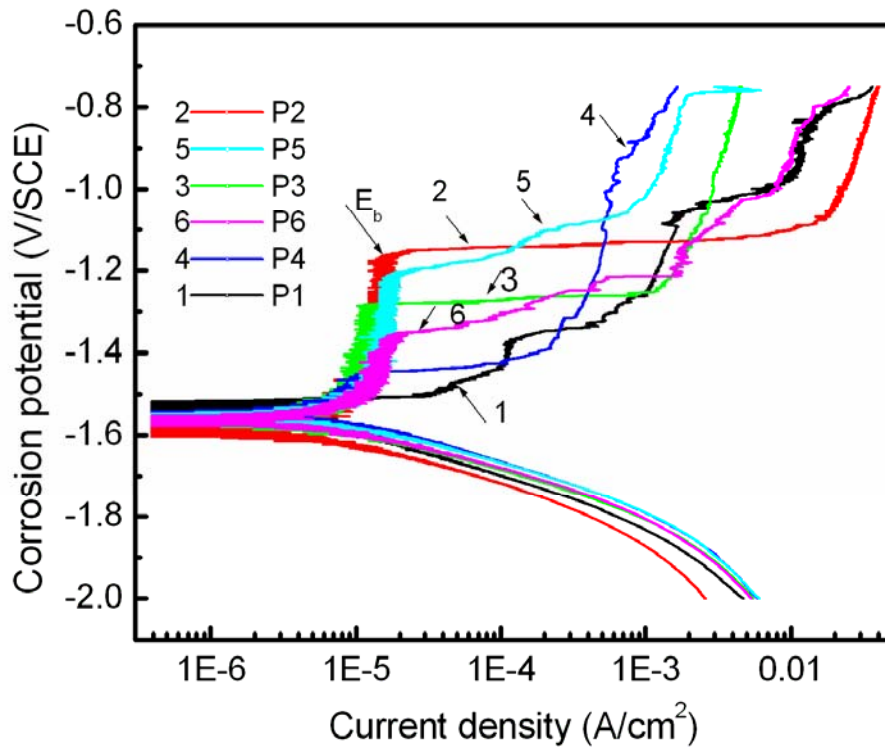


Fig.12

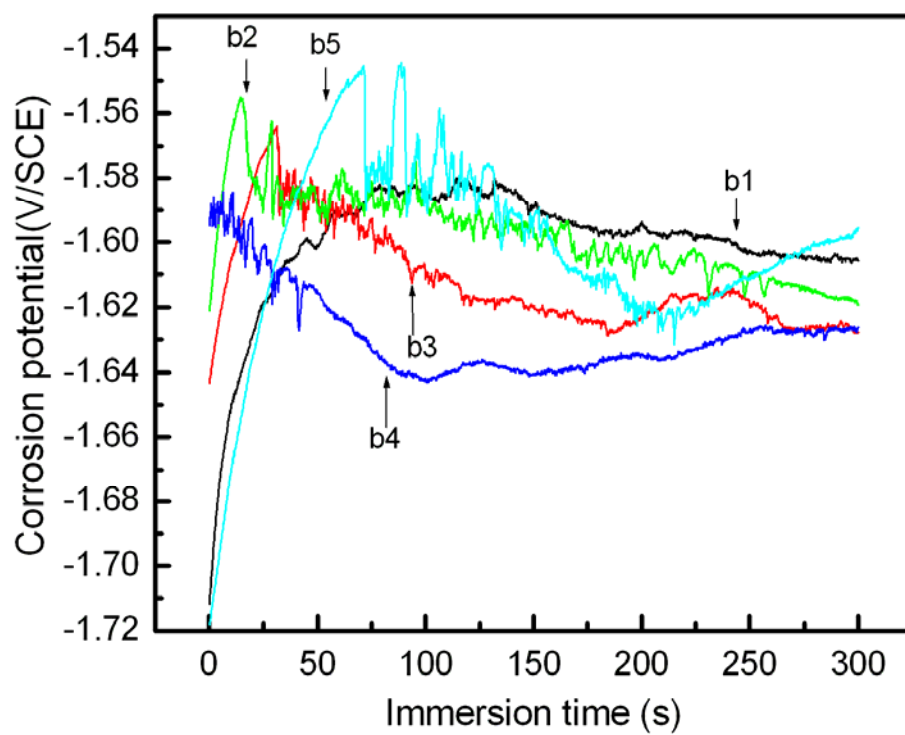


Fig.13

